

Date of publication xxxx 00, 0000, date of current version xxxx 00, 0000.

Digital Object Identifier 10.1109/ACCESS.2021.Doi Number

A Novel Simplified Implementation of Finite-Set Model Predictive Control for Power Converters

Jose J. Silva¹, Jose R. Espinoza¹, Senior Member, IEEE, Jaime A. Rohten², Member, IEEE, Esteban S. Pulido³, Felipe A. Villarroel¹, Marcos L. Andreu¹.

¹Department of Electrical Engineering, Universidad de Concepción, Victor Lamas 1290, Región del Bío-Bío 4070386, Chile.

²Department of Electrical and Electronic Engineering, Universidad del Bío-Bío, Avenida Collao 1202, Región del Bío-Bío 4051381, Chile.

³Department of Electrical Engineering, Universidad Técnica Federico Santa María, Avenida España 1680, Valparaíso 2390123, Chile.

Corresponding author: Jaime A. Rohten (e-mail: jrohten@ubiobio.cl).

This work was supported by the Chilean Government under Project CONICYT/FONDECYT/11170407, CONICYT-PCHA/Doctorado Nacional/2016-21161547, ANID / FONDAP / SERC/ /15110019, ANID / FONDEQUIP / EQM 140148, and the Advanced Center for Electrical and Electronics Engineering AC3E (ANID/FB0008).

ABSTRACT This paper presents a novel simplified method to implement the finite set - model predictive control technique for photovoltaic generation systems connected to the *ac* network. This method maintains the advantages of the conventional finite set - model predictive control, such as fast response, simple implementation, and easy understanding; but it also eliminates the use of a cost function and hence the weighting factors, instead, it finds the optimal operating state directly from the model and the discrete number of valid states of the converter. Although the proposed algorithm does not compute a cost function, it is able to select the inverter state that minimizes the tracking error by using a hexagonal convergence region. The main advantage of this technique is to reduce the computational cost in 43% of the algorithm that selects the best state, presenting a simple and complete algorithm without compromising the predictive control performance. The proposed algorithm properly operates under various conditions such as changes in the network frequency and changes in the system parameters.

INDEX TERMS Predictive control, Solar power generation, *ac-dc* power converters, Fast MPC.

I. INTRODUCTION

Renewable energy is an extensively studied topic in many worldwide research centers, because of the need to find new energy sources to replace traditional polluting ones such as oil or coal, to mention some of them [1]. Solar energy is particularly interesting because it is available in almost any place and not hard to harvest. However, in order to make this energy competitive with traditional ones, many researchers have put their efforts to improve the operation of the different stages of photovoltaic (PV) plants, including some applications as the electric vehicles [2], [3]. Therefore, the study has been mostly divided into the Maximum Power Point Tracking (MPPT) algorithms, in the power converter stage, using a *dc/dc* converter or only a inverter, and the proper control of these power converters [3], [4]. In this context of clean energy, the current work is placed on analyzing and proposing a simplified method of controlling power converters to inject solar energy to the grid, *i.e.*, in the power converter stage.

Solar energy is available worldwide and can be collected through photovoltaic cells. The intensity of solar radiation (S)

and temperature (T) are different in each geographic location and change along the day [5]. Solar irradiance and operating temperature are critical variables in solar photovoltaic systems because the amount of energy that can be collected is directly dependent on them. Monofacial solar panels are widely used in big PV plants; but it has been demonstrated that bifacial photovoltaic (BPV) modules achieve higher efficiency [6], [7] and are increasingly being used in PV plants, minimizing the construction area. For this reason, this work will focus on using the BPV technology.

In order to maximize the production of photovoltaic systems, several MPPT algorithms have been developed to find the maximum power point. The most used algorithms are incremental conductance (InC) [8], disturbance and observation (P&O) [9], and measuring cell based (MCB) [10], [11]. These MPPTs have been implemented in *dc/dc* converters [7], directly in the inverter control strategy [12], where the MPPT imposes the *dc* link voltage, eliminating the additional *dc/dc* stage and, therefore, the total efficiency is increased. In order to inject the electrical energy generated by the BPV cell array this work will use the active front-end

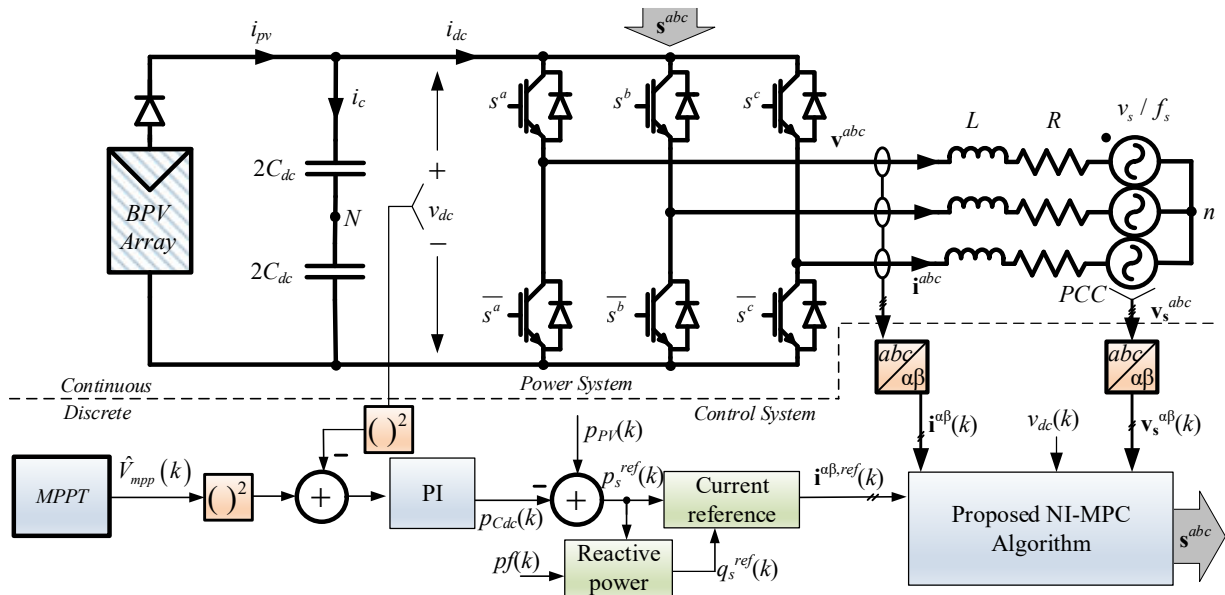


FIGURE 1. NPC Grid tie inverter using BPV Cells including control scheme.

(AFE) topology [13]. The proposed control strategy will be divided in 3 stages: (i) MPPT algorithm (to get the most power of the BPV array), (ii) linear dc voltage control (to adjust the dc voltage required by the MPPT), and (iii) model predictive control (MPC), such as finite set - model predictive control (FS-MPC), to control the current injected into the power grid.

The main contribution of this paper is the proposition of a new way to implement the MPC technique for AFE converters [14]. As conventional FS-MPC, the focus is on reaching the reference in a minimum number of steps and keeping the results and advantages of the conventional FS-MPC algorithm. However, the proposed method avoids the cost function definition and the iterations to evaluate all possible states, thus reducing the computational burden.

As reported in the literature [15], [16], the computational cost for the FS-MPC is high and grows up with the number of combinations (states), being the main disadvantage of this control technique. Thus, many simplifications have been reported in order to reduce the amount of operation the microcomputer must do [16]–[18]. The proposed method, named No-Iteration-MPC (NI-MPC), divides the chart of the possible states in hexagons around every valid state to define clear regions where the desired voltage, given by the control scheme, is placed. Thus the NI-MPC has the advantages of the FS-MPC, but avoiding iterations, and therefore maintaining the high performance of MPC compared with classical methods as the hysteresis current control, linear current control among others [16], [19]. The proposed power converter control is designed to extract the maximum energy coming from a BPV matrix and inject it into the electrical network.

One advantage of the proposed NI-MPC is the possibility to extend the algorithm for multilevel converter, where the timing improvement is even more notable. This is because as the number of levels increases, the number of state's combinations increases significantly, which directly affects

the traditional FS-MPC, since it must evaluate each state during its optimization process, which is not done by the proposed NI-MPC. In NI-MPC, this can be done directly by defining the region around every state, as shown later. In addition, this control method has not restrictions on the middle point voltage regulation, just like traditional FS-MPC, and can be employed for both, current control and voltage balancing.

The provided simulated and experimental results show satisfactory response in a photovoltaic injection system, corroborating the theoretical analysis, with fast dynamic response and suitable steady-state performance for the proposed NI-MPC algorithm.

II. MATHEMATICAL MODEL

A. Power Converter Model

The power converter model of the system can be found easily thanks to the Kirchhoff's laws. Thus, the ac side topology mathematical representation of FIGURE 1 can be found as:

$$\mathbf{v}^{abc} = L \frac{d}{dt} \mathbf{i}^{abc} + R \mathbf{i}^{abc} + \mathbf{v}_s^{abc}. \quad (1)$$

The voltage to be injected can be written as function of the switching pattern as:

$$\mathbf{v}^{abc} = \frac{1}{2} \mathbf{s}^{abc} v_{dc} + \mathbf{1} v_{Nn}, \quad (2)$$

with v_{Nn} the voltage between the middle point in the dc capacitors (N) and the neutral wire (n), $\mathbf{1} = [1 \ 1 \ 1]^T$, and $\mathbf{s}^{abc} = [s^a \ s^b \ s^c]^T$, where the switch states values can be either -1 or 1. Then, using (1) and (2), the voltage v_{Nn} can be found as:

$$v_{Nn} = \frac{1}{3} \left(L \frac{d}{dt} \langle \mathbf{i}^{abc}, \mathbf{1} \rangle + R \langle \mathbf{i}^{abc}, \mathbf{1} \rangle + \langle \mathbf{v}_s^{abc}, \mathbf{1} \rangle - \frac{1}{2} v_{dc} \langle \mathbf{s}^{abc}, \mathbf{1} \rangle \right) \quad (3)$$

where $\langle \cdot, \cdot \rangle$ represents the dot product. On the other hand, the dc side is mathematically modeled by the Kirchhoff's current law as:

$$i_{pv} = C \frac{dv_{dc}}{dt} + i_{dc} = C \frac{dv_{dc}}{dt} + \frac{1}{2} \langle \mathbf{i}^{abc}, \mathbf{s}^{abc} + \mathbf{1} \rangle \quad (4)$$

The *ac* filter is designed to fulfill two main requirements: fast dynamic response and low THD current. The first requirement imposes a maximum inductance value:

$$L \leq f_1(I_{\max}, V_{s,\max}, V_{dc}), \quad (5)$$

where I_{\max} is the maximum current, $V_{s,\max}$ is the maximum grid voltage and V_{dc} is the *dc* operating voltage, [20]. The second one imposes a minimum inductance value as a function of the current THD:

$$L \geq f_2(\text{THD}(i)). \quad (6)$$

Thus, the filter selection is a trade-off between dynamic response and the quality of the current waveform, [21]. In the case of the NI-MPC, the current harmonic content is distributed, as shown later, and does not exist a dominant harmonic, therefore the THD must be found from the results. The imposed conditions for this work are a current THD less than 5%, fitting the IEEE standard 519 [22], and reach the maximum required current.

B. Discrete $\alpha\beta$ Power Converter Model

The $\alpha\beta$ reference frame is commonly employed for power converters as most systems can be considered balanced in amplitude and phase, and points N and n are isolated. Therefore, the set of equations are reduced from three (*abc*) to two ($\alpha\beta$), and the control design results simpler. The Clarke's Transformation will be defined as:

$$\vec{u}^{\alpha\beta} = \sqrt{2/3} (u^a + \bar{z}u^b + \bar{z}^2u^c), \quad (7)$$

where $\bar{z} = e^{j2\pi/3}$, $u^a + u^b + u^c = 0$ and $\vec{u}^{\alpha\beta} = u^\alpha + ju^\beta$. Then, the vector $\mathbf{u}^{\alpha\beta}$ is defined as:

$$\mathbf{u}^{\alpha\beta} = \left[\text{Re}\{\vec{u}^{\alpha\beta}\} \quad \text{Im}\{\vec{u}^{\alpha\beta}\} \right]^T. \quad (8)$$

Employing the Euler's approximation, the equations (1) and (4) are depicted as:

$$\begin{aligned} \mathbf{i}^{abc}(k+1) &\approx \\ \hat{\mathbf{i}}^{abc}(k+1) &= \left(1 - \frac{T_s}{L}R\right) \mathbf{i}^{abc}(k) + \frac{T_s}{L} (\mathbf{v}^{abc}(k) - \mathbf{v}_s^{abc}(k)), \quad (9) \end{aligned}$$

$$\begin{aligned} v_{dc}(k+1) &\approx \\ \hat{v}_{dc}(k+1) &= v_{dc}(k) + \frac{T_s}{C} i_{pv}(k) - \frac{T_s}{C} \frac{1}{2} \langle \hat{\mathbf{i}}^{abc}(k), \mathbf{s}^{abc}(k) + \mathbf{1} \rangle, \quad (10) \end{aligned}$$

where $\hat{\mathbf{i}}^{abc}(k+1)$ and $\hat{v}_{dc}(k+1)$ are the estimated or predicted variables at $k+1$. Thus, there is a clear relationship between the variables to estimate the future values as function of the actual ones by considering the mathematical representation of (7) and (8).

C. BPV array model

The BPV matrix shown in **FIGURE 1** is based on the series connection of N_s cells that form a string, and N_p strings connected in parallel. Each cell is electrically modeled using the Single Diode Model (SDM) [23], where the electrical circuit is shown in **FIGURE 2**. The parameters of the electrical model of the cell are series resistance R_s ; shunt resistance R_{sh}

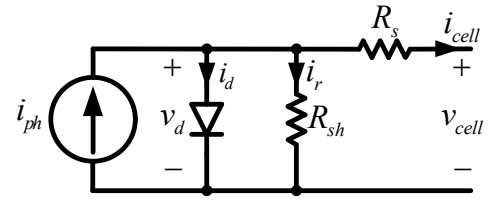


FIGURE 2. Equivalent electrical circuit of a BPV cell model.

(the resistors represent the losses of the cell); ideality factor n (also called emission coefficient, which is around 2 for crystalline silicon, and is less than 2 for amorphous silicon); nominal short-circuit current I_{sco} ; the reverse saturation current of the diode I_o ; the electron charge q and Planck's constant k . **Table 1** summarizes the parameters of a typical BPV cell.

The BPV array considered in this work can generate 250 kW operating under standard test conditions (STC), *i.e.*, irradiance $S_0 = 1000 \text{ W/m}^2$, temperature $T_0 = 25 \text{ }^\circ\text{C}$ and air mass $AM = 1.5$. If all cells are electrically equal and operate with the same temperature (T) and the same irradiance (S), the power generated by the BPV array can be calculated with the following equations:

$$P_{pv} = i_{pv} v_{dc} = f(T, S, v_{dc}), \quad (11)$$

$$i_{pv} = I_{sco} \frac{S}{S_o} N_p - I_o N_p \left(e^{\left(\frac{v_d^T / N_s}{nkT} \right) q} - 1 \right) - \frac{v_d^T / N_s}{R_{sh} N_p}, \quad (12)$$

where,

$$v_d^T = v_{dc} + \frac{N_s R_s i_{pv}}{N_p}. \quad (13)$$

The MPPT algorithm gives the voltage reference to the inverter's control, where the voltage reference comes from the measuring cell MPPT based method. This MPPT algorithm is fully detailed in [10], [11] which uses the cell model to estimate the maximum power point and voltage by employing two measuring cells. One cell in open circuit and a second one in short circuit, where two internal PI controllers regulate the variables, based on the model, to reach the temperature and the MPP voltage, which provides the *dc* voltage reference for the power control.

Table 1. BPV Array Parameters

Parameter	Value
N_s / N_p	1560 cells / 39 cells.
R_s / R_{sh}	0.0035 Ω / 1000 Ω
I_{sco} / I_o	8.58 A / 2.16×10^{-8} A
n	1.2 p.u.

III. ACTIVE AND REACTIVE POWER CONTROL

The MPPT control, as shown in **FIGURE 1**, provides the *dc* voltage reference that needs to be tracked by the converter. Moreover, the converter has the capability to compensate reactive power by phase-shifting the current.

On the first hand, the provided energy by the solar array (p_{pv}) supplies the power to charge the *dc* capacitor (p_{Cdc}), the power losses at the inductive *ac* filter (p_{filter}), and the power injected to the grid (p_s). Thus, the equation that represents this relationship is given by:

$$P_{PV} = P_{Cdc} + P_{filter} + P_s. \quad (14)$$

Commonly, the power related to the filter use, P_{filter} , is very low, therefore, it can be neglected as an approximation. The power related to dc capacitor is given by a PI controller that allows to track the dc voltage reference:

$$P_{Cdc}(k) = P_{Cdc}(k-1) + k_1 e^{vdc}(k) + k_2 e^{vdc}(k-1), \quad (15)$$

where k_1 and k_2 are the PI controller parameters, and

$$e^{vdc}(k) = (v_{dc}^{ref}(k))^2 - (v_{dc}(k))^2. \quad (16)$$

The power P_s is taken as the reference value, leading to:

$$P_s^{ref}(k) = P_{PV}(k) - P_{Cdc}(k). \quad (17)$$

On the other hand, the reactive power reference is usually imposed by the displacement power factor (dpf) required at the point of common coupling (PCC). The dpf is associated to the angle:

$$\theta_{vi}(k) = \pm \cos^{-1}(dpf(k)), \quad (18)$$

where its sign depends on if the dpf is inductive or capacitive. Thus, the reactive power reference is defined as:

$$q_s^{ref}(k) = P_s^{ref}(k) \tan(\theta_{vi}(k)). \quad (19)$$

Using both, the active and reactive power, the current reference can be calculated as a function of the reference power and the sensed voltage supply as:

$$\mathbf{i}^{\alpha\beta,ref}(k) = \frac{1}{\|\mathbf{v}_s^{\alpha\beta}(k)\|^2} \begin{bmatrix} \text{Re}\{(P_s^{ref}(k) - jq_s^{ref}(k))\bar{\mathbf{v}}_s^{\alpha\beta}(k)\} \\ \text{Im}\{(P_s^{ref}(k) - jq_s^{ref}(k))\bar{\mathbf{v}}_s^{\alpha\beta}(k)\} \end{bmatrix}. \quad (20)$$

The complete control scheme is shown in **FIGURE 1**.

IV. PREDICTIVE CURRENT CONTROL

The FS-MPC is nowadays, in the academic literature, a very popular way to track current and power references, these types of controllers do not need to be tuned and, in general, have much faster dynamics than the response of linear controllers [24]. However, to properly control power converters a high sampling frequency is commonly employed [25]–[27], and additionally, FS-MPC requires to consider all possible states into the sampling time and select the one that minimizes the cost functional, aspects which lead to a high computational burden. Instead, in this section is proposed the key concept of the new NI-MPC method to improve this drawback. The mathematical model, crucial in MPC algorithms, was established in Section II, and will be used to control the currents, and the active and reactive power.

A. Proposed NI-MPC Current Control

The proposed NI-MPC control technique permits to manage the currents avoiding iterations. This algorithm is simpler, and at the same time, conserves the advantages of the traditional FS-MPC. The first step is to find the voltage that the converter needs to inject in order to reach the reference two steps forward. The converter voltage is defined from (5), (6) and (9) as:

$$\mathbf{v}^{\alpha\beta}(k+1) = \frac{L}{T_s} \mathbf{i}^{\alpha\beta}(k+2) + \left(R - \frac{L}{T_s}\right) \hat{\mathbf{i}}^{\alpha\beta}(k+1) + \hat{\mathbf{v}}_s^{\alpha\beta}(k+1) \quad (21)$$

where (9) has been one step forwarded because of the digital board computing delay. To calculate (21) it is required to

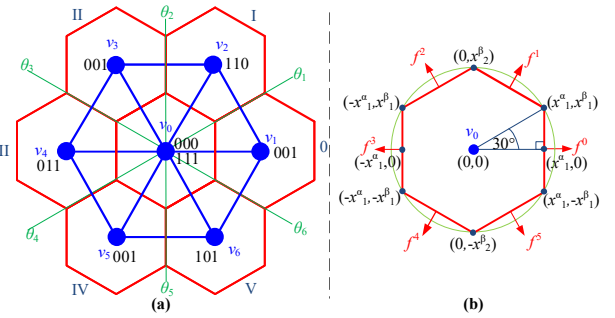


FIGURE 3. Valid states for the power converter (a) all 8 states, (b) highlighting the three nearest voltages for a given voltage $v^{\alpha\beta}$.

compute $\hat{\mathbf{i}}^{\alpha\beta}(k+1)$ and $\hat{\mathbf{v}}_s^{\alpha\beta}(k+1)$. Meanwhile, the reference is set to be $\mathbf{i}^{\alpha\beta}(k+2) = \mathbf{i}^{\alpha\beta,ref}(k+2)$, which is obtained using (18). In (21), the current prediction is given by:

$$\hat{\mathbf{i}}^{\alpha\beta}(k+1) = \left(1 - \frac{T_s}{L} R\right) \mathbf{i}^{\alpha\beta}(k) + \frac{T_s}{L} (\hat{\mathbf{v}}_s^{\alpha\beta}(k) - \mathbf{v}_s^{\alpha\beta}(k)), \quad (22)$$

and the voltage $\mathbf{v}_s^{\alpha\beta}(k+1)$ can be estimated by a Lagrange approximation as the grid voltage is a sinusoidal waveform:

$$\hat{\mathbf{v}}_s^{\alpha\beta}(k+1) = 3\mathbf{v}_s^{\alpha\beta}(k) - 3\mathbf{v}_s^{\alpha\beta}(k-1) + \mathbf{v}_s^{\alpha\beta}(k-2). \quad (23)$$

Therefore, the injected voltage at $k+1$ has to be synthesized considering the seven valid converter voltages (**FIGURE 1**). To apply this voltage, and to avoid iterations, it is proposed to split the total voltage region in seven areas, as represented in **FIGURE 3** (a), where the separation is achieved by the hexagons which isolate every single valid voltage. Once the desired voltage to be injected is known, the valid state closest to the voltage reference is chosen and applied at the next step. To achieve this, seven identical hexagons are defined and centered in every valid voltage v_x (with $x = 0, \dots, 6$). A zoom of the hexagon surrounding the voltage v_0 is shown in **FIGURE 3** (b), where the hexagon border lines are defined by functions f^j ($j = 0, \dots, 5$) that are employed to divide the areas around every valid state v_x . All the hexagon border line functions in **FIGURE 3** (b) are calculated as follows. The ordinate axis is defined as ‘ x^β ’ and the abscissa axis as ‘ x^α ’. In **FIGURE 3** (b) $x_1^\alpha = 1/2$, $x_1^\beta = 1/(2\sqrt{3})$, $x_2^\beta = 1/\sqrt{3}$, and the slope m of f^1 and f^4 are the same and given by:

$$m^{1,4} = -x_1^\alpha / \cos(30) = -1/\sqrt{3}. \quad (24)$$

On the other hand, the slope of f^2 and f^5 are equal to $m^{1,4}$ but negative, i.e., $m^{2,5} = -m^{1,4}$, therefore, all the border lines are known and characterized by the functions f^0, f^1, \dots, f^5 , or in rectangular coordinates as $f^l: x^\beta = m^l x^\alpha + b^l$ ($l = 0, 1, \dots, 5$), which can be defined as:

$$\begin{aligned} f^0: & x^\alpha = 1/2, x^\beta \in [-1/2, 1/2] \\ f^1: & x^\beta = -x^\alpha / \sqrt{3} + 1/\sqrt{3} \\ f^2: & x^\beta = x^\alpha / \sqrt{3} + 1/\sqrt{3} \\ f^3: & x^\alpha = -1/2, x^\beta \in [-1/2, 1/2] \\ f^4: & x^\beta = -x^\alpha / \sqrt{3} - 1/\sqrt{3} \\ f^5: & x^\beta = x^\alpha / \sqrt{3} - 1/\sqrt{3} \end{aligned} \quad (25)$$

In order to employ the $\alpha\beta$ voltage reference given by the predictive control in (21), the border lines in FIGURE 3 (b) f^j are transformed to polar coordinates using the mapping $x^\alpha = r \cdot \cos(\theta)$, $x^\beta = r \cdot \sin(\theta)$, with r and θ the magnitude and angle of the respective vector. Applying the transformation to the functions defined in (23) is obtained:

$$\begin{aligned} f^0 : & \quad x^\alpha = r^0 \cos(\theta) \\ f^1 : & \quad r^1 \sin(\theta) = -r^1 \cos(\theta) / \sqrt{3} + 1 / \sqrt{3} \\ f^2 : & \quad r^2 \sin(\theta) = r^2 \cos(\theta) / \sqrt{3} + 1 / \sqrt{3} \\ f^3 : & \quad x^\alpha = r^3 \cos(\theta) \\ f^4 : & \quad r^4 \sin(\theta) = -r^4 \cos(\theta) / \sqrt{3} - 1 / \sqrt{3} \\ f^5 : & \quad r^5 \sin(\theta) = r^5 \cos(\theta) / \sqrt{3} - 1 / \sqrt{3} \end{aligned} \quad (26)$$

where r^j and θ represent the magnitude and angle of the corresponding voltage reference, respectively. Thus, each border line can also be written as:

$$\begin{aligned} r^0 &= \frac{1/2}{\cos(\theta)}, r^1 = \frac{1/2}{\sin(\theta+30)}, \\ r^2 &= \frac{1/2}{\sin(\theta-30)}, r^3 = \frac{-1/2}{\cos(\theta)}, \\ r^4 &= \frac{-1/2}{\sin(\theta+30)}, r^5 = \frac{-1/2}{\sin(\theta-30)}. \end{aligned} \quad (27)$$

Once the control generates the reference voltage $\bar{v}^{\alpha\beta} = v^\alpha + jv^\beta$ using (21), the closest one is chosen among all valid the states. In fact, the proposed algorithm determines in which hexagon the reference voltage is located by choosing the one in the middle v_x . First, it needs the reference voltage in polar coordinates, which can be easily found as $\bar{v}^{\alpha\beta} = \|\mathbf{v}^{\alpha\beta}\| e^{j\theta}$, where:

$$\|\mathbf{v}^{\alpha\beta}\| = \sqrt{\langle \mathbf{v}^{\alpha\beta}, \mathbf{v}^{\alpha\beta} \rangle}, \quad (28)$$

$$\theta = \arg(\bar{v}^{\alpha\beta}). \quad (29)$$

Then, the first step is to determine the zone where the reference voltage is located (zone 0, I, II, ..., V). Afterwards, it is verified if the voltage reference is inside or outside the central hexagon, FIGURE 3 (b), using the ratios defined in (27) in the latter case. The algorithm follows the sequence illustrated in FIGURE 4, in order to select the optimum state to apply, where the box "into the center hexagon?" requires the parametrization of all line functions previously developed, (25) and (26). The complete flow-chart of the NI-MPC algorithm is shown in FIGURE 5.

V. COMPUTATIONAL EFFORT AND COMPARISON BETWEEN THE NI-MPC AND FS-MPC

The proposed NI-MPC algorithm is able to select the state to apply without using a cost function when compared to the traditional FS-MPC (FIGURE 6), which evaluates each state (8 times for this converter) and selects the optimum one ($s_{opt}^{\alpha\beta}$) that minimizes the cost functional (g). The Table 2 presents the computational cost required for both algorithms, i.e., the operations necessary to implement the

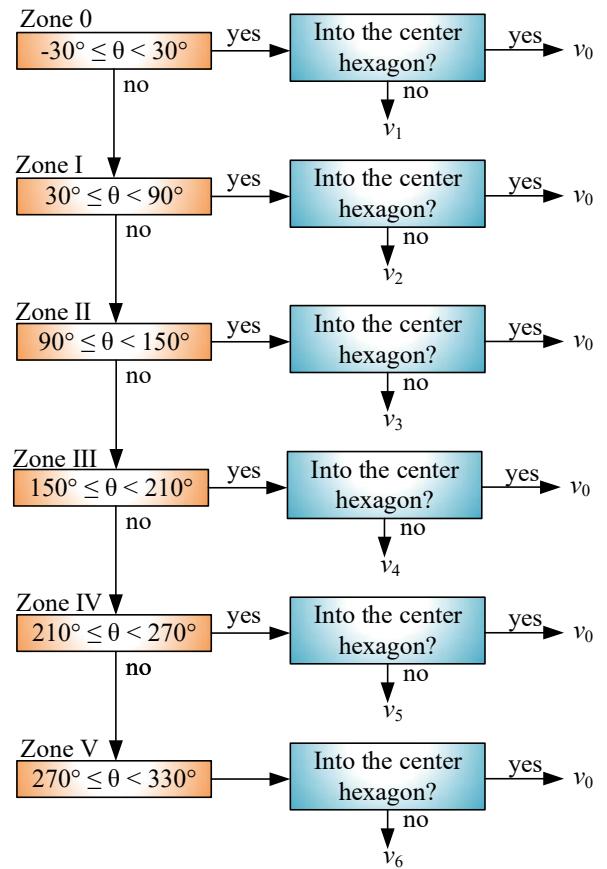


FIGURE 4. NI-MPC Algorithm to decide the state to be applied.

traditional FS-MPC and the proposed NI-MPC algorithm, where acquisition, PLL, Clarke Transform and state writing times are not considered, since these stages are the same for both algorithms. Table 2 also shows the computation time for each operation considering the DSP-based board TMS320F28335 [28] to highlight the difference in the total computation time. The proposed NI-MPC algorithm is faster than the traditional one and provides very similar results in terms of dynamics and harmonic content as will be shown below. As this algorithm converges to the same

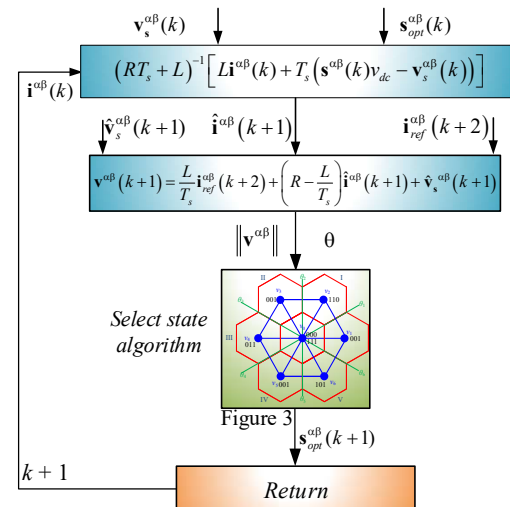


FIGURE 5. Proposed NI-MPC algorithm flow-chart.

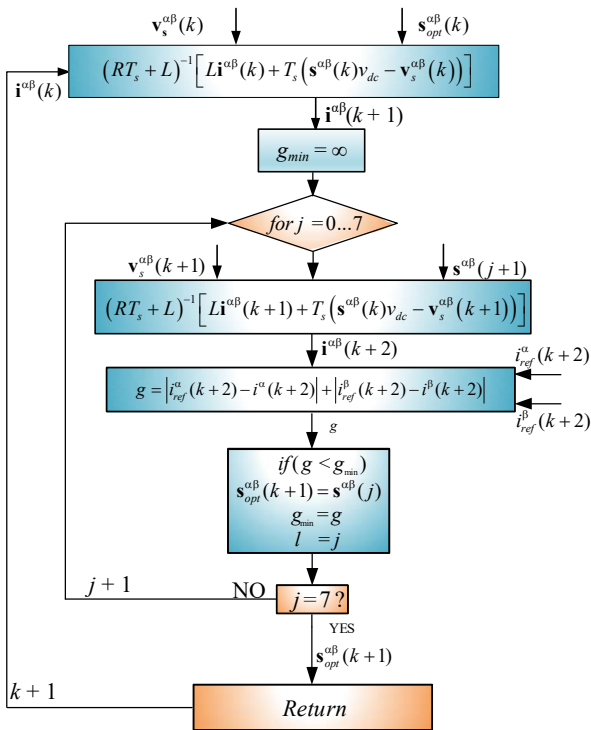


FIGURE 6. Traditional FS-MPC algorithm flow-chart.

solution as the traditional FS-MPC, the losses associated with the topology are the same as those obtained with the FS-MPC [29]. Table 3 summarizes the differences and similarities of the proposed NI-MPC and the traditional FS-MPC.

Table 2. Computational effort

Algorithm	Operation	Number of operations	Time to evaluate
FS-MPC	Sums	26	26.7 ns×26
	Subtractions	25	33.4 ns×25
	Multiplications	27	60.0 ns×27
	Magnitude	16	280 ns×2
	For, if, and other instructions	17	26.7 ns×17
	Total Time		
NI-MPC	Sums	10	26.7 ns×10
	Subtractions	10	33.4 ns×10
	Multiplications	23	60.0 ns×23
	Divisions	4	220 ns×4
	For, if, and other instructions	7	26.7 ns×7
	acos(-)	1	410 ns×1
	sin(-)	2	410 ns×2
	Magnitude	1	280 ns×1
Total Time			4.56 μs

Table 3. Comparison between the Ni-MPC and FS-MPC

Comparison	Parameter	FS-MPC	NI-MPC
Differences	Number of iterations	8	1
	Cost function	Yes	No
	Computer time	8.08 μs	4.56 μs
Similarities	PWM/SVM modulation	No	No
	Response time	fast	fast
	THD ₁	<5%	<5%
	Harmonic content	Spread spectrum	Spread spectrum
	T _s (controller sampling time)	55.5 μs	55.5 μs

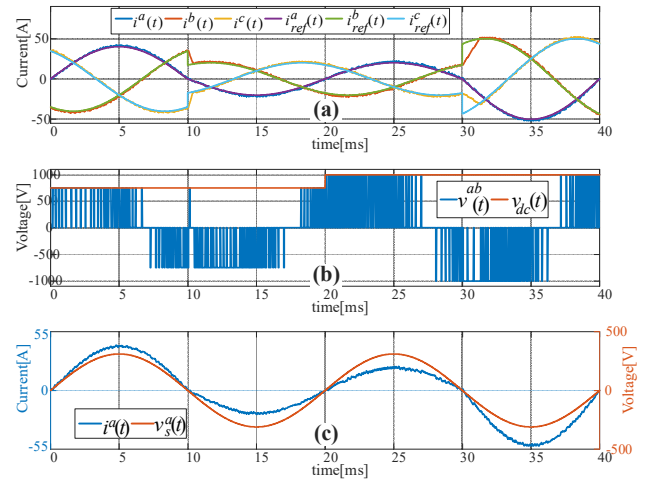


FIGURE 7. Simulated current test of NI-MPC. (a) Output Currents $i^{abc}(t)$ and their references. (b) Output voltage $v^{ab}(t)$ and DC link voltage $v_{dc}(t)$. (c) Current and voltage of the phase a at the grid: $i^a(t)$ and $v_s^a(t)$.

VI. Results

In order to verify the proposed control, the system is tested under simulations and experimentally. The PV system is implemented by a solar emulator Magna Power SL 600/4.3v which considers irradiance and temperature as disturbances to be imposed, which leads to changes in the maximum power point (M_{pp}) curve, forcing the system to track it by changing the dc voltage.

Table 4. Simulation Parameters

Parameter	Value
R (filter resistance)	0.03 Ω
L (filter inductance)	0.5 mH
C_{dc} (dc -filter capacitance)	4.7 mF
V_s (rms nominal ac -voltage supply)	220 V
P_{MPP} (power at STC)	250 kW
f_s (nominal frequency supply)	50 Hz
T_s (controller sampling time)	55.5 μs

A. Current Control Test

The test shown in FIGURE 7 (a) presents the results of the simulation of the $i^{abc}(t)$ and $i_{ref}^{abc}(t)$ currents. The simulating parameters are listed in Table 4. The references amplitudes are changed at $t = 10ms$ from 40[A] to 10[A] and at $t = 30ms$ from 20[A] to 50[A]. In both changes the proposed NI-MPC is able to track the reference in a very short period of time. FIGURE 7 (b) shows the dc voltage $v_{dc}(t)$, and the output voltage of the converter $v^{ab}(t)$, where at $t = 20ms$ a step-up change in $v_{dc}(t)$ is made. The control does not lose track of the reference; in fact, it does look to be unaffected by this step change. Finally, FIGURE 7 (c) shows the voltage and current of phase a , showing that the system operates with a unitary displacement power factor ($dpf = 1$) as expected. FIGURE 8 shows the step response in the d axis, illustrating the fast dynamics of the current control, as it is able to reach the reference in less than 1 ms. This because it takes the

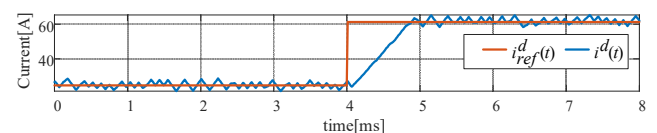


FIGURE 8. Step response. (a) Output Current $i^d(t)$ and its reference.

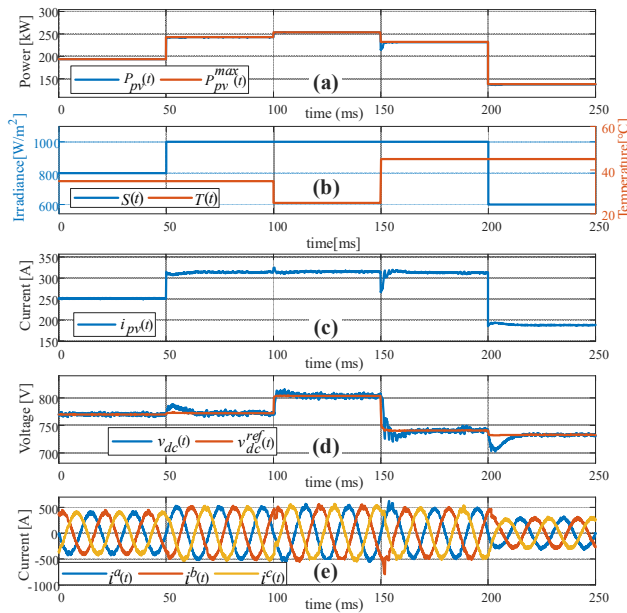


FIGURE 9. Simulated test of the whole system using NI-MPC. (a) Generated power $p_{pv}(t)$ and the theoretic maximum power p_{pv}^{max} , (b) Environmental conditions: radiation $S(t)$ and temperature $T(t)$, (c) Generated current of the PV array $i_{pv}(t)$, (d) DC link voltage $v_{dc}(t)$ and its reference $v_{dc}^{ref}(t)$ (e) Output Currents $i^{abc}(t)$.

shortest path to reach the reference, being just limited by the power converter dynamics.

B. Complete System Test

The results presented in **FIGURE 9** show the response obtained from the simulation of the complete PV system. **FIGURE 9** (a) shows the power generated by the BPV array, which changes every 50ms due to environmental conditions. In **FIGURE 9** (b), the first 50ms have an irradiance of 800W/m^2 , reducing the maximum power that can be generated; from 50ms to 100ms the irradiance reaches the nominal value S_o , but the temperature is 35°C , which also reduces the generation capacity; and, from 100ms to 150ms, the PV farm operates in nominal conditions S_o and T_o , therefore the arrangement is capable of generating the designed 250kW .

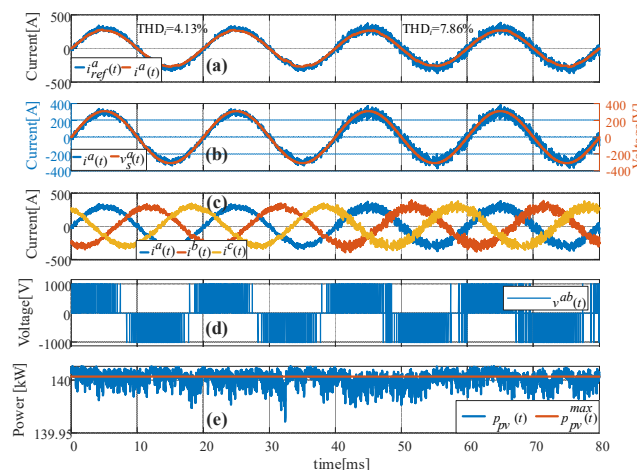


FIGURE 10. Simulated test parameter change, reducing L . (a) Output current $i^a(t)$ and its reference $i_{ref}^a(t)$, (b) Current and voltage of the phase a at the grid: $i^a(t)$ and $v_s^a(t)$, (c) Output currents $i^{abc}(t)$, (d) Output voltage $v^{ab}(t)$, (e) Generated power $p_{pv}(t)$ and the theoretic maximum power $p_{pv}^{max}(t)$.

In the next 50ms the temperature rises again, and the power is reduced, as in the last 50ms, where the irradiance decreases to 600W/m^2 .

FIGURE 9 (c) presents the current generated by the BPV array, which is directly related to the irradiance of **FIGURE 9** (b) i.e., if the irradiance increases, the current increases and vice versa. **FIGURE 9** (d) shows the operating voltage of the BPV array, which varies according to environmental changes. It can be noticed that this variable is more related to the temperature, contrary to the current, which is related with the irradiance, as stated before. **FIGURE 9** (e) shows the currents injected into the grid (i^{abc}); their amplitude is proportional to the generated p_{pv} .

From the results, it can be concluded that the algorithm can generate a correct voltage reference under the different conditions. In fact, the system tracks the maximum theoretical power, neglecting transient differences due to the dynamics of the DC controller and the electrical system.

C. Robustness Tests

In order to study the robustness of the proposed NI-MPC, changes are applied to the parameters, as seen in **FIGURE 10** and **FIGURE 11**. The parameters are kept constant into the control algorithm and the change is only due to the converter filter and power system.

In the test shown in **FIGURE 10** the inductance L is reduced down to 50% of its nominal value, where it can be seen that the control system is able to track the given current reference, operating close to the M_{PP} and with unitary dpf . In this case, the current THD is calculated according the IEEE standard [22], [30] considering up to the 51st harmonic, where it can be seen an increment from 4.13% to 7.86% because of the inductor reduction. In **FIGURE 11** the inductor size is increased up to 200%, and therefore, the THD decreases from 4.13% to 2.63%. Finally, **FIGURE 12** shows the NI-MPC output current and voltage harmonic content, where it is important to highlight the similarity in the spread on these harmonics, such as the FS-MPC. The NI-MPC maximum switching frequency is 18kHz ($1/T_s$), however, the switching frequency is not fixed, **FIGURE 12**, hence there

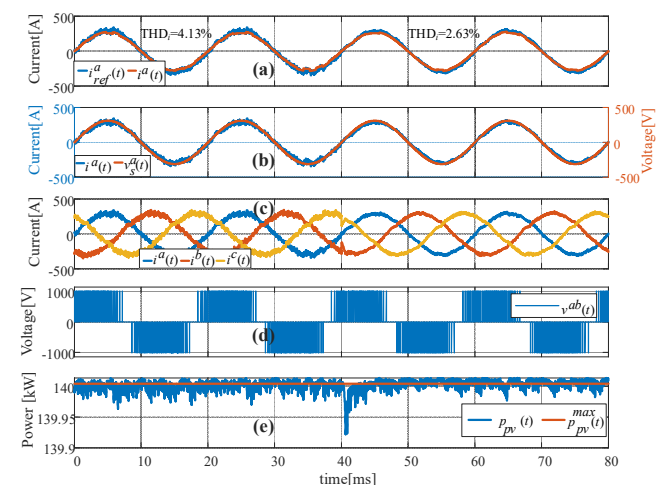


FIGURE 11. Simulated test parameter change, increasing L . (a) Output current $i^a(t)$ and its reference $i_{ref}^a(t)$, (b) Current and voltage of the phase a at the grid: $i^a(t)$ and $v_s^a(t)$, (c) Output currents $i^{abc}(t)$, (d) Output voltage $v^{ab}(t)$, (e) Generated power $p_{pv}(t)$ and the theoretic maximum power $p_{pv}^{max}(t)$.

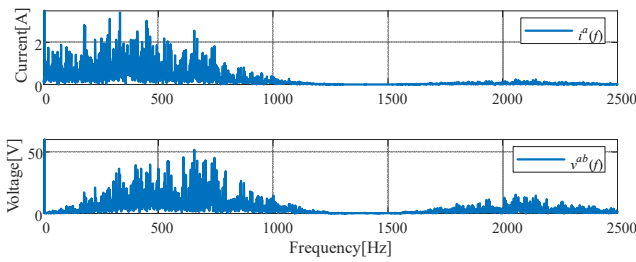


FIGURE 12. Harmonic content. (a) Current $i^a(f)$, (b) Grid voltage $v_s^a(f)$.

is no dominant harmonic, just like the FS-MPC, because the NI-MPC also chooses the state in order to follow the shortest path to the reference. In this context, the power converter losses for the proposed NI-MPC are identical as compared to the traditional FS-MPC, where a complete analysis can be found in the literature [31]–[33], which is also valid for this algorithm.

Table 5. Experimental Parameters

Parameter	Value
R (filter resistance)	0.5 Ω
L (filter inductance)	2 mH
C_{dc} (dc-filter capacitance)	2.35 mF
V_s (rms nominal ac-voltage supply)	30 V
V_{MPP} (dc-voltage at STC)	120 V
f_s (nominal frequency supply)	50 Hz
P (nominal inverter's power)	500 W
P_{MPP} (Power at STC)	350 W
T_s (controller sampling time)	55.5 μ s

D. Experimental Results

The tests performed in the experimental setup, using the system parameters shown in Table 5, are now presented. The current loop was tested against disturbances on the electrical network. The results are depicted in Figure 13, imposing a unitary displacement power factor and a constant v_{dc} voltage. The first test, Figure 13 (a), shows the system response against an increase of the mains frequency, from 50Hz to 100Hz, that is not expected in practice but serves to

indeed test the algorithm. Although the current is affected by this change, the controller rapidly takes the current to its unitary displacement power factor and the voltage is unaffected by this important frequency change. Figure 13 (b) & (c) shows the control response to voltage amplitude changes in the electrical network, sag for Figure 13 (b) and swell for Figure 13 (c). It can be seen that in both cases a unitary displacement power factor is maintained and, again, the v_{dc} voltage control is unaffected, properly rejecting the imposed disturbances.

In order to further test the designed PI v_{dc} controller, a change in the v_{dc} reference is performed, Figure 13 (d). It can be seen that the voltage increases from 80V to 120V approximately in less than 300ms, and although the power generated increases, the current injected into the mains remains in phase with the mains voltage. To complete the tests for the control scheme, Figure 13 (e) presents a dpf change. The current is shifted in time, first lagging, and then leading with respect to the grid voltage, passing from $dpf = 0.8$ capacitive to $dpf = 0.8$ inductive. This is an important result because it shows that the proposed control scheme can allow reactive power injection into the grid to help for system stability, particularly in the system voltage.

Finally, the PV system was tested using the PV Magna Power SL 600/4.3v emulator. Five power profiles were designed to emulate solar generation changes due to environmental changes as shown in Figure 14 (a). To perform this test, the profiles are changed every 10 seconds, saving data such as power, voltage and current from the emulator. Figure 14 (b) shows the power injected and how it changes along the time due to the imposed disturbances in the temperature and irradiance. Figure 14 (c) shows the dc current generated by the photovoltaic arrangement for the different power profiles. Figure 14 (d) shows how the control system adjusts the dc voltage reference in order to track the M_{pp} , where the power control must track the voltage reference. Finally, Figure 14 (e) shows how the dc voltage is

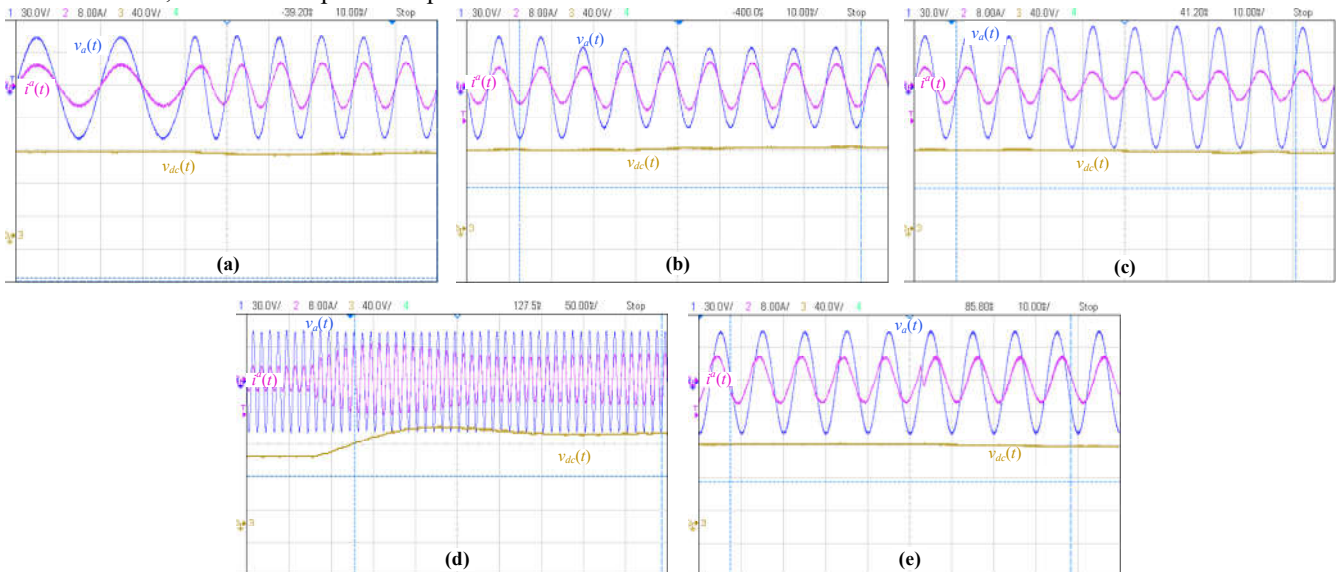


FIGURE 13. Experimental test under grid disturbances. (a). Grid frequency increase. (b) Grid amplitudes decrease. (c) Grid amplitudes increase. Top current and voltage of the phase a at the grid: $i^a(t)$ and $v_s^a(t)$ bottom dc link voltage $v_{dc}(t)$, (d) dc link voltage $v_{dc}(t)$ test, top current and voltage of the phase a at the grid: $i^a(t)$ and $v_s^a(t)$ bottom dc link voltage $v_{dc}(t)$. (e) Displacement power factor test, top current and voltage of the phase a at the grid: $i^a(t)$ and $v_s^a(t)$ bottom dc link voltage $v_{dc}(t)$.

adjusted to reach the M_{pp} of the different power profiles. It can be seen that the system is able to follow the M_{pp} and stays close to this operation point.

VII. CONCLUSIONS

This paper has presented a new method to implement a non-modulated MPC maintaining fast dynamic, robustness under parameters changes and disturbances, and easy implementation, but using less computational effort than the conventional FS-MPC algorithm. The proposed NI-MPC is based on eliminating the iteration steps of FS-MPC with a more direct implementation. A direct selection of the power converter states using hexagonal regions of convergence is proposed to achieve this objective. The definition of the regions can be obtained systematically employing the mathematical representation of the converter states chart. Afterwards, the reference voltage is located in the corresponding hexagon. The response of the proposed NI-MPC algorithm was found to be very similar to the FS-MPC response, i.e., with a spread spectrum and taking the shortest path to the reference. The experimental results show that NI-MPC is capable to track current references allowing to control the dc voltage and the displacement power factor, operating in the maximum power point in solar systems.

The implementation of NI-MPC for multilevel power converters as used in higher power PV systems can be easily extended. In these converters, the number of levels complicate the implementation of the traditional FS-MPC, because the number of states is high, leading to excessive computation time. Instead, the proposed NI-MPC considerably reduces the computational effort by avoiding the traditional iteration procedure.

REFERENCES

- [1] A. Qazi *et al.*, "Towards Sustainable Energy: A Systematic Review of Renewable Energy Sources, Technologies, and Public Opinions," *IEEE Access*, vol. 7, pp. 63837–63851, 2019, doi: 10.1109/ACCESS.2019.2906402.
- [2] P. S. Subudhi, K. Subramanian, and B. B. J. D. Retnam, "WIRELESS ELECTRIC VEHICLE BATTERY-CHARGING SYSTEM FOR SOLAR-POWERED RESIDENTIAL APPLICATIONS," *Int. J. Power Energy Syst.*, vol. 39, no. 3, 2019, doi: 10.2316/J.2019.203-0116.
- [3] P. S. Subudhi and K. S., "Wireless Power Transfer Topologies used for Static and Dynamic Charging of EV Battery: A Review," *Int. J. Emerg. Electr. Power Syst.*, vol. 21, no. 1, Feb. 2020, doi: 10.1515/ijeeps-2019-0151.
- [4] L. Alpuerto and R. S. Balog, "Comparing Connection Topologies of PV Integrated Curved Roof Tile for Improved Performance," in *2020 IEEE Texas Power and Energy Conference (TPEC)*, Feb. 2020, pp. 1–5, doi: 10.1109/TPEC48276.2020.9042523.
- [5] F. Wang, Z. Li, X. Tong, and L. Chen, "Modeling, Analysis and Evaluation of Modified Model Predictive Control Method for Parallel Three-Level Simplified Neutral Point Clamped Inverters," *IEEE Access*, vol. 7, pp. 185349–185359, 2019, doi: 10.1109/ACCESS.2019.2961054.
- [6] L. Burnham, D. Riley, B. Walker, and J. M. Pearce, "Performance of Bifacial Photovoltaic Modules on a Dual-Axis Tracker in a High-Latitude, High-Albedo Environment," in *2019 IEEE 46th Photovoltaic Specialists Conference (PVSC)*, Jun. 2019, pp. 1320–1327, doi: 10.1109/PVSC40753.2019.8980964.
- [7] A. Neubert, M. Hamer, R. A. Kharait, and M. A. Mikofski,

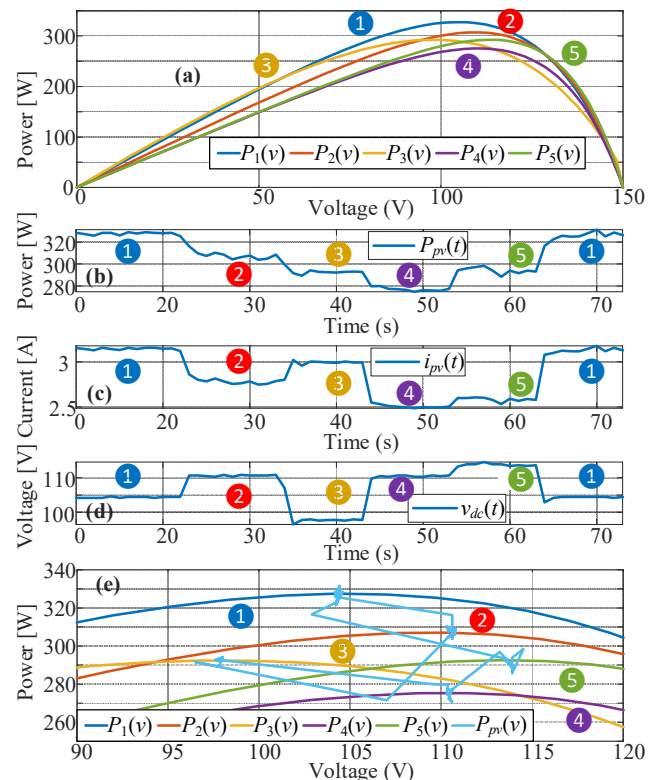


FIGURE 14. Experimental test, PV system results. (a) Photovoltaic profiles P_{pv} with respect to v_{dc} . (b) Experimental $P_{pv}(t)$. (c) Experimental $v_{dc}(t)$. (d) Experimental $i_{pv}(t)$, (e) Experimental $P_{pv}(v_{dc})$ and photovoltaic profiles.

- [8] M. Alsumiri, "Residual Incremental Conductance Based Nonparametric MPPT Control for Solar Photovoltaic Energy Conversion System," *IEEE Access*, vol. 7, pp. 87901–87906, 2019, doi: 10.1109/ACCESS.2019.2925687.
- [9] P. Jiang and X. You, "Improved variable step size perturbation observation MPPT algorithm based on linear auto disturbance rejection," in *2019 Chinese Automation Congress (CAC)*, Nov. 2019, pp. 5495–5500, doi: 10.1109/CAC48633.2019.8996812.
- [10] J. Silva, J. Espinoza, M. Torres, J. Rohten, C. Baier, and J. Munoz, "Global Maximum Power Point Tracking Scheme on a Partially Shaded Photovoltaic Array," in *IECON 2018 - 44th Annual Conference of the IEEE Industrial Electronics Society*, Oct. 2018, pp. 1830–1834, doi: 10.1109/IECON.2018.8591320.
- [11] R. Morales *et al.*, "Grid Connected PV System with New MPPT Estimation Method Based on Measuring Cells," *IECON Proc. (Industrial Electron. Conf.)*, vol. 2019-October, no. 2, pp. 2366–2371, 2019, doi: 10.1109/IECON.2019.8927843.
- [12] J. J. Silva *et al.*, "MPC Algorithm With Reduced Computational Burden and Fixed Switching Spectrum for a Multilevel Inverter in a Photovoltaic System," *IEEE Access*, vol. 8, pp. 77405–77414, 2020, doi: 10.1109/ACCESS.2020.2988627.
- [13] J. A. Rohten, J. E. Muñoz, E. S. Pulido, J. J. Silva, F. A. Villarroel, and J. R. Espinoza, "Very Low Sampling Frequency Model Predictive Control for Power Converters in the Medium and High-Power Range Applications," *Energies*, vol. 14, no. 1, p. 199, Jan. 2021, doi: 10.3390/en14010199.
- [14] J. A. Rohten *et al.*, "Enhanced Predictive Control for a Wide Time-Variant Frequency Environment," *IEEE Trans. Ind. Electron.*, vol. 63, no. 9, pp. 5827–5837, Sep. 2016, doi: 10.1109/TIE.2016.2541625.
- [15] M. Norambuena, C. Garcia, J. Rodriguez, and P. Lezana, "Finite Control Set Model Predictive Control reduced computational cost applied to a Flying Capacitor converter," in *IECON 2017 -*

- 43rd Annual Conference of the IEEE Industrial Electronics Society, Oct. 2017, pp. 4903–4907, doi: 10.1109/IECON.2017.8216846.
- [16] Changliang Xia, Tao Liu, Tingna Shi, and Zhanfeng Song, “A Simplified Finite-Control-Set Model-Predictive Control for Power Converters,” *IEEE Trans. Ind. Informatics*, vol. 10, no. 2, pp. 991–1002, May 2014, doi: 10.1109/TII.2013.2284558.
- [17] Y. Zhang and H. Lin, “Simplified model predictive current control method of voltage-source inverter,” in *8th International Conference on Power Electronics - ECCE Asia*, May 2011, pp. 1726–1733, doi: 10.1109/ICPE.2011.5944459.
- [18] M. Siami, D. Arab Khaburi, and J. Rodriguez, “Simplified Finite Control Set-Model Predictive Control for Matrix Converter-Fed PMSM Drives,” *IEEE Trans. Power Electron.*, vol. 33, no. 3, pp. 2438–2446, Mar. 2018, doi: 10.1109/TPEL.2017.2696902.
- [19] J. Rodriguez *et al.*, “Predictive Current Control of a Voltage Source Inverter,” *IEEE Trans. Ind. Electron.*, vol. 54, no. 1, pp. 495–503, Feb. 2007, doi: 10.1109/TIE.2006.888802.
- [20] E. S. Pulido *et al.*, “Design and Implementation of a Parallel-Connected Fault Current Attenuator for Power Distribution Systems,” *IEEE J. Emerg. Sel. Top. Power Electron.*, pp. 1–1, 2021, doi: 10.1109/JESTPE.2021.3081048.
- [21] P. Karamanakos and T. Geyer, “Guidelines for the Design of Finite Control Set Model Predictive Controllers,” *IEEE Trans. Power Electron.*, vol. 35, no. 7, pp. 7434–7450, Jul. 2020, doi: 10.1109/TPEL.2019.2954357.
- [22] “IEEE Standard Definitions for the Measurement of Electric Power Quantities Under Sinusoidal, Nonsinusoidal, Balanced, or Unbalanced Conditions,” *IEEE Std 1459-2010 (Revision IEEE Std 1459-2000)*, pp. 1–50, 2010, doi: 10.1109/IEEESTD.2010.5439063.
- [23] J. Johnson, D. Yoon, and Y. Baghzouz, “Modeling and analysis of a bifacial grid-connected photovoltaic system,” in *2012 IEEE Power and Energy Society General Meeting*, Jul. 2012, pp. 1–6, doi: 10.1109/PESGM.2012.6345266.
- [24] M. Tomlinson, T. Mouton, and R. Kennel, “Finite-control-set model predictive control with a fixed switching frequency vs. linear control for current control of a single-leg inverter,” in *2015 IEEE International Symposium on Predictive Control of Electrical Drives and Power Electronics (PRECEDE)*, Oct. 2015, pp. 109–114, doi: 10.1109/PRECEDE.2015.7395592.
- [25] M. A. Perez, Ricardo Lizana Fuentes, and J. Rodriguez, “Predictive control of DC-link voltage in an active-front-end rectifier,” in *2011 IEEE International Symposium on Industrial Electronics*, Jun. 2011, pp. 1811–1816, doi: 10.1109/ISIE.2011.5984432.
- [26] L. Qiu, X. Liu, J. Sun, J. Zhang, J. Ma, and Y. Fang, “Fast Finite-Set Model Predictive Control for Three-Phase Four-Arm Active Front End Modular Multilevel Converters Under Unbalanced and Distorted Network Conditions,” *IEEE Access*, vol. 8, pp. 30504–30514, 2020, doi: 10.1109/ACCESS.2020.2970474.
- [27] M. Safaeian, A. Jalilvand, and A. Taheri, “A MRAS Based Model Predictive Control for Multi-Leg Based Multi-Drive System Used in Hot Rolling Mill Applications,” *IEEE Access*, vol. 8, pp. 215493–215504, 2020, doi: 10.1109/ACCESS.2020.3041310.
- [28] M. P. Kazmierkowski, M. Jasinski, and G. Wrona, “DSP-Based Control of Grid-Connected Power Converters Operating Under Grid Distortions,” *IEEE Trans. Ind. Informatics*, vol. 7, no. 2, pp. 204–211, May 2011, doi: 10.1109/TII.2011.2134856.
- [29] R. Hariri, F. Sebaaly, and H. Y. Kanaan, “Comparative Analysis of Predictive Control Systems Applied to a Grid-Tied NPC Inverter,” in *2019 IEEE International Conference on Industrial Technology (ICIT)*, Feb. 2019, pp. 1195–1201, doi: 10.1109/ICIT.2019.8755193.
- [30] D. M. F. G. Roger, *IEEE Recommended Practice and Requirements for Harmonic Control in Electric Power Systems*, vol. 2014. 2014.
- [31] M. Alhasheem, T. Dragicevic, M. Rivera, and F. Blaabjerg, “Losses evaluation for a two-level three-phase stand-alone voltage source converter using model predictive control,” in *2017 IEEE Southern Power Electronics Conference (SPEC)*, Dec. 2017, pp. 1–6, doi: 10.1109/SPEC.2017.8333624.
- [32] B. Gadalla, E. Schaltz, Y. Siwakoti, and F. Blaabjerg, “Thermal performance and efficiency investigation of conventional boost, Z-source and Y-source converters,” in *2016 IEEE 16th International Conference on Environment and Electrical Engineering (EEEIC)*, Jun. 2016, pp. 1–6, doi: 10.1109/EEEIC.2016.7555610.
- [33] J. Munoz, C. Baier, J. Espinoza, M. Rivera, J. Guzman, and J. Rothen, “Switching losses analysis of an asymmetric multilevel Shunt Active Power Filter,” in *IECON 2013 - 39th Annual Conference of the IEEE Industrial Electronics Society*, Nov. 2013, pp. 8534–8539, doi: 10.1109/IECON.2013.6700565.